Supplementary Information

Molecularly Engineered, Multifunctional Imide Derivatives for Practical Zn Metal Full Cells

Shengyang Huang[a,‡], Peng Zhang[a,‡], Jun Lu[a], Jun Su Kim[a], Dong Hyun Min[a], Jin Suk Byun[a], Min Ju Kim[a], Hao Fu[a], Peixun Xiong[a], Pil J. Yoo[a], Wenwu Li[a], Xu Yu[b], Xue Qin[c], and Ho Seok Park[a,d,e,*]

[a] School of Chemical Engineering, Sungkyunkwan University, 2066, Seoburo, Jangan-gu, Suwon 440-746, Republic of Korea

[b] School of Chemistry and Chemical Engineering, Yangzhou University, Yangzhou, 225002, China

[b] Department of Chemistry, School of Science, Tianjin University, Tianjin, 300072, China

[d] Department of Health Sciences and Technology, Samsung Advanced Institute for Health Sciences and Technology (SAIHST), Sungkyunkwan University, 2066, Seoburo, Jangan-gu, Suwon, 440-746, Republic of Korea

[e] SKKU Institute of Energy Science and Technology (SIEST), Sungkyunkwan University, 2066, Seoburo, Jangan-gu, Suwon 440-746, Republic of Korea

Corresponding authors: phs0727@skku.edu (H. S. Park)

1. Experimental Section:

Electrolyte preparation

A 2 M baseline electrolyte of $ZnSO_4$ was prepared by dissolving $ZnSO_4 \cdot H_2O$ (Alfa Aesar, >99.9%) in deionized water (DI water, homemade). To create the electrolyte for the cells, succinimide (H-SU, Alfa Aesar, 98+%) was added into the as-prepared 2 M $ZnSO_4$ pristine electrolyte at various concentrations. For comparison, control groups were also prepared by adding N-Hydroxysuccinimide (OH-SU, NHS, Sigma-Aldrich, 98%), N-Methylsuccinimide (CH_3-SU, NMS, Sigma-Aldrich, 99%), N-Chlorosuccinimide (Cl-SU, NCS, Sigma-Aldrich, 98%) at a concentration of 100 mM into the 2 M $ZnSO_4$ electrolyte.

Cathodes preparation and Cell fabrication

The polyaniline (PANI) cathodes were fabricated by combining 70 wt% of PANI powder (Sigma-Aldrich, average Mw ~100000), 15 wt% carbon black (CB, Alfa Aesar), 5% wt% multi-walled carbon nanotubes (US Research Nanomaterials, Inc.) and 10 wt% sodium carboxymethylcellulose (CMC, Sigma-Aldrich, average Mw ~250000) in DI water. The resulting slurry was cast on carbon paper and left to dry at 80 °C for 3 h. This process yielded cathodes with a PANI loading of approximately ~2.0 mg cm^{-2}.

A novel co-precipitation method was employed to synthesize manganese vanadate (MnVO). 60 mg of V_2O_5 (Sigma-Aldrich, ≥ 98%) was added to 14 mL of water, followed by the addition of 1.5 mL of H_2O_2, and stirred until clear. Then, 30 mg of $MnSO_4 \cdot H_2O$ was added and uniformly dissolved. Nitrogen was purged into the system and sealed. After sealing, the system was aged at 80 °C for 24 h to obtain MnVO powder. The cathodes were prepared by blending 70 wt% of active materials, 20 wt% Ketjen Black (KB, Lion Specialty Chemicals Co., Ltd.), and 10 wt% polyvinylidene fluoride (PVDF, Sigma-Aldrich, average Mw ~180000) in 1-methyl-2-pyrrolidone (NMP, DAEJUNG). The resulting slurry was cast onto a titanium foil and dried at 80 °C overnight, yielding a MnVO loading of approximately 4.0 mg cm^{-2} on each cathode.

The MoO_x@TiO_2 powder was synthesized through an in-situ coating and solvent thermal method. Initially, 0.5 g MoO_3 powder (Sigma-Aldrich, ≥ 99.5%) was dispersed evenly in 200 mL ethanol.

Then, 0.82 g titanium tetraisopropoxide (TTIP, Junsei Chemical Co., Ltd., 98%) was added and stirred at 100 ℃ for 1 h. After washing and centrifugation, the composite was calcined at 600 ℃ for 14 h to obtain MoO_x@TiO_2 powder. MoO_x@TiO_2 cathodes were prepared by blending 70 wt% of MoO_x@TiO_2 powder, 20 wt% CB, and 10 wt% PVDF in NMP. The slurry was cast on Ti foil and dried at 80 °C overnight, resulting in a MoO_x@TiO_2 loading of ~2.0 mg cm^{-2} in each cathode. All of cathodes were confirmed by XRD spectra (Fig. S27).

The free-standing ultrahigh loading cathode with ultrahigh loading of ~60 mg cm^{-2} is fabricated by casting the slurry on a glass slide and left to dry at 80 °C overnight. After drying, the free-standing ultra-high loading cathode can be removed and used directly.

The Zn||Zn symmetric cells were assembled in the CR2032 coin-type cells under an ambient atmosphere. Zn foils (Alfa Aesar, thickness 250 μm) were mechanically rolled to 40 μm and punched to Φ10 mm to serve as the electrodes, with glass fiber (Whatman, GF/A, Φ16 mm) as the separator and 100 μL electrolyte. The Zn||Cu asymmetric cells were identical to Zn||Zn symmetric cells, except one Zn electrode was replaced with a Cu electrode (Φ10 mm). Full cells consisted of Zn anodes, the aforementioned cathodes, and 100 μL electrolyte. For low n/p ratio full cells, the Zn foils were specially continuously rolled to 20 μm and combined with the free-standing ultrahigh loading cathode.

Material characterizations

The surface and morphological characteristics of Zn electrodes were thoroughly investigated using various analytical techniques. Fourier-transform infrared (FT-IR) spectra were recorded using an FT-IR 4700 instrument (JASCO) and adopted an attenuated total reflection (ATR) method. Raman spectra were recorded using a Confocal Raman Spectrometer (NT-MDT) with a wavelength of 532 nm. X-ray diffraction (XRD) patterns were recorded using an X-ray diffractometer (PANalytical, Almelo) with Cu Kα radiation (λ = 0.154 nm). For the characterization of the surface components of electrodes, X-ray photoelectron spectroscopy (XPS, ESCALAB 250, Thermo-Scientific) was employed. Depth-dependent XPS spectra were obtained by etching the Zn surface with Ar^+ sputtering for 0 s, 300 s, 600 s, and 900 s. The binding energies of XPS spectra were

determined by reference to the adventitious C 1s peak at 284.6 eV. The nuclear magnetic resonance (NMR) samples were meticulously prepared by dissolving $ZnSO_4$ (and the additive) in deuterium oxide (D_2O) containing 0.75 wt.% 3-(trimethylsilyl) propionic-2,2,3,3-d4 acid sodium salt (TSP) as the internal standard. The ^{1}H NMR and ^{13}C NMR spectra were recorded on a 700 MHz spectrometer (AVANCE III 700, Bruker). Scanning electron microscopy (SEM, JSM-7000F, JEOL) was employed to examine the morphologies. A 3D measuring laser confocal scanning microscope (3D LCSM, OLS5100, Olympus) was utilized for the three-dimensional imaging and reconstruction of Zn samples. Atomic force microscopy (AFM) was conducted on NX10 (Park Systems). Time-of-flight secondary ion mass spectrometry (TOF-SIMS) measurements were conducted using a TOF-SIMS-5 (ION-TOF). Sputtering was performed using a 1 keV O_2 beam over a 150×150 μm^2 area, and the analysis area was 40×40 μm^2 using a pulsed 25 keV Bi^+ primary beam. UV-vis absorption spectra were obtained by MULTISKAN GO (Thermo SCIENTIFIC). To evaluate the ionic conductivities and pH value of the electrolytes, a conductivity/pH meter (SevenMulti, Mettler-Toledo) was used.

Electrochemical measurements

To investigate the electrochemical properties, cyclic voltammetry (CV), linear sweep voltammetry (LSV), electrochemical impedance spectroscopy (EIS) measurements and chronoamperometry (CA) were performed using a BioLogic VMP3 Multichannel Potentiostat. Plating and stripping tests for (a)symmetric cells were then conducted on the WonATech WBCS3000L automatic battery test system and the Maccor Series 4000 automated battery test system. To gain insights into the electrochemical behavior of the symmetric cells, EIS measurements were conducted over a wide frequency range spanning from 10 Hz to 100 kHz. For CV analysis, a two-electrode cell configuration was utilized with Cu and Zn foils serving as the working and counter electrodes, respectively. The CV curves were scanned over a voltage range of -0.2 to 0.4 V at a sweep rate of 1 mV s^{-1}. Monitoring of the hydrogen evolution reaction (HER) was performed using LSV in a 2 M Na_2SO_4 aqueous solution with/without 100 mM additive, at a sweep rate of 5 mV s^{-1}. The ESW was tested by SS||SS sets from three-electrode systems. The CA method was employed to record

diffusion curves with an overpotential of 150 mV. Corrosion tests were carried out in a three-electrode setup in a 2 M $ZnSO_4$ electrolyte with and without 100 mM additive. The working and counter electrodes were Zn foils. The reference electrode is silver chloride (Ag/AgCl). The measurement of the transference number of Zn^{2+} (t_{Zn}) was conducted in symmetric cells with two Zn electrodes. This procedure involved EIS and CA with an applied voltage of 10 mV for a duration of 10 min. Subsequently, the cells were allowed to stand for 12 h before data recording. The t_{Zn} value was calculated using Eq. 1:

$$t_{Zn} = \frac{I_s(\Delta V - I_0 R_0)}{I_0(\Delta V - I_s R_s)} \quad (1)$$

where ΔV represents the applied potential (10 mV), I_0 and Is are the initial and steady-state currents, respectively. Additionally, R_0 and Rs donate the initial and steady-state electrode resistances, respectively. The differential capacitance-potential curves of the Zn||Cu asymmetric cells were obtained using the Mott-Schottky method within the voltage range of 0.3-1.0 V. The galvanostatic intermittent titration technique (GITT) measurements were conducted within the working voltage range of the corresponding cathodes. The curves were obtained by applying a constant current pulse for 5 min, followed by relaxation periods of 30 min.

Calculation methods

The density functional theory (DFT) was conducted using the CASTEP code within Materials Studio program to investigate the effect of additives on the Zn surface based on first-principles calculations. The Perdew-Burke-Ernzerhof (PBE) based on generalized-gradient approximation (GGA) was employed to handle exchange and correlation effects. A four-atom layer unit constituting the (002) slab was established using lattice constant information. Each slab was given a vacuum spacing of 15 Å along the Z-axis direction to prevent mutual interference. Throughout the calculation process, the cut-off energy was set at 400 eV. To ensure accurate calculation of electronic properties, the Brillouin zone was sampled using k-points with a (2, 2, 1) grid. Furthermore, convergence tolerances for geometry optimization calculations were set to a

maximum displacement of 0.001 Å, a maximum energy change of 1.0×10^{-5} eV atom^{-1}, and a self-consistent field (SCF) convergence tolerance of 1.0×10^{-6} eV atom^{-1}. During the geometry optimization process, the lower two layers of atoms in the Zn slab model were fixed, while the top two layers and added parts were allowed to relax until the maximum force acting on each atom was less than 0.05 eV Å^{-1}. The adsorption energy (ΔE) between the Zn slab and additive was calculated using Eq. 2:

$$\Delta E = E_{all} - E_{adsorbent} - E_{adsorbate} \quad (2)$$

Here, the adsorbate is the surface of the Zn (002) plane. The adsorbent is H_2O and additive.

The binding energy (ΔE_b) between Zn^{2+} and H_2O/SU^- were calculated using Eq. 3:

$$\Delta E_b = E_{all} - E_{Zn^{2+}} - E_{H_2O/SU^-} \quad (3)$$

The molecular dynamics (MD) simulations were conducted using the Forcite code within Materials Studio to investigate the solvation structure of Zn^{2+}. A model electrolyte comprising H_2O: $ZnSO_4$: Additive = 2775:100:10 with a density of 1.33 g cm^{-3} was packed into a periodic box. Energy minimization was then performed using the steepest descent algorithm with a force tolerance of 0.005 kcal mol^{-1} Å^{-1}. Subsequently, the system was relaxed for 1 ns using the NPT ensemble. Following these preparation steps, 12 ns NPT MD simulations were carried out at 298 K under a pressure of 1 bar, employing a time step of 1 fs. The last 6 ns frame rate was selected to compute radial distribution functions.

2. Supplemental Figures and Tables:

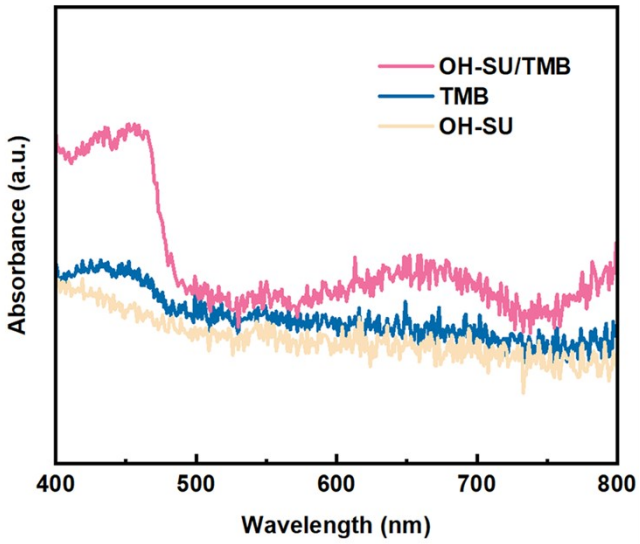

Fig. S1 UV-vis spectra of OH-SU/TMB, TMB and OH-SU.

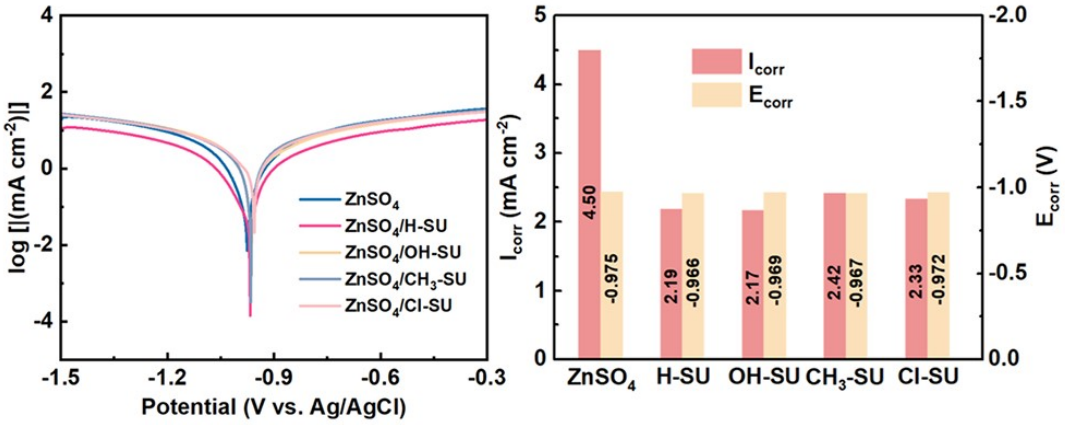

Fig. S2 Tafel curves of different electrolytes and related corrosion values.

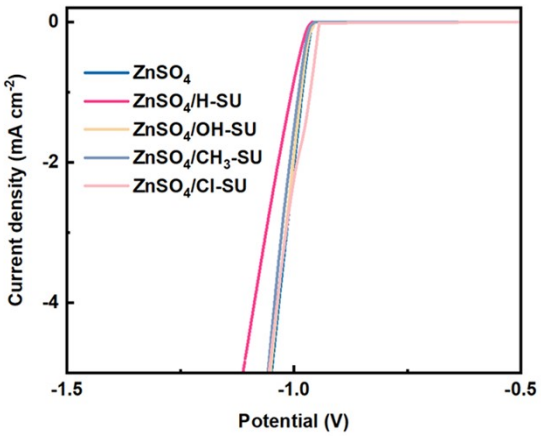

Fig. S3 LSV curves of different electrolytes.

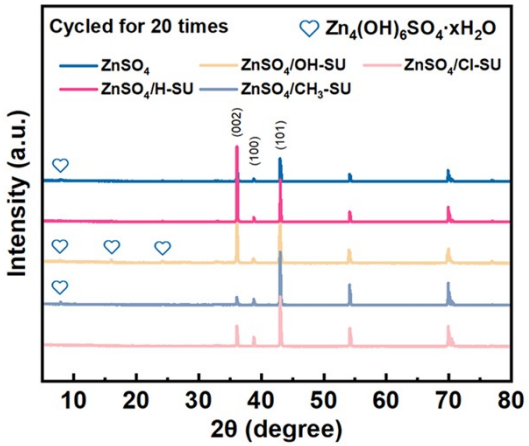

Fig. S4 XRD spectra of Zn cycled after 20 times in $ZnSO_4$ and $ZnSO_4$/x-SU electrolytes.

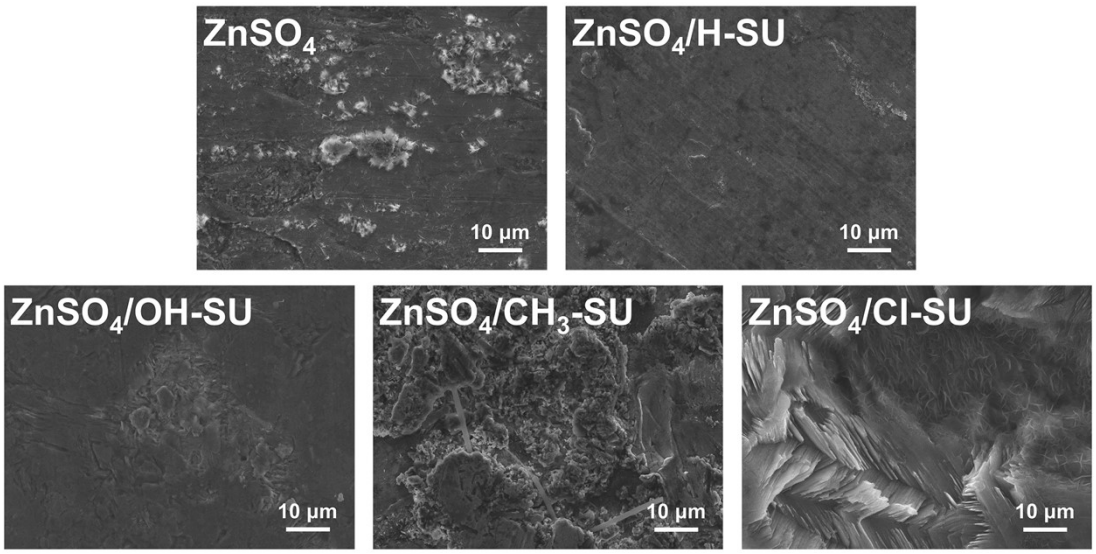

Fig. S5 SEM image of Zn cycled after 20 times in different electrolytes.

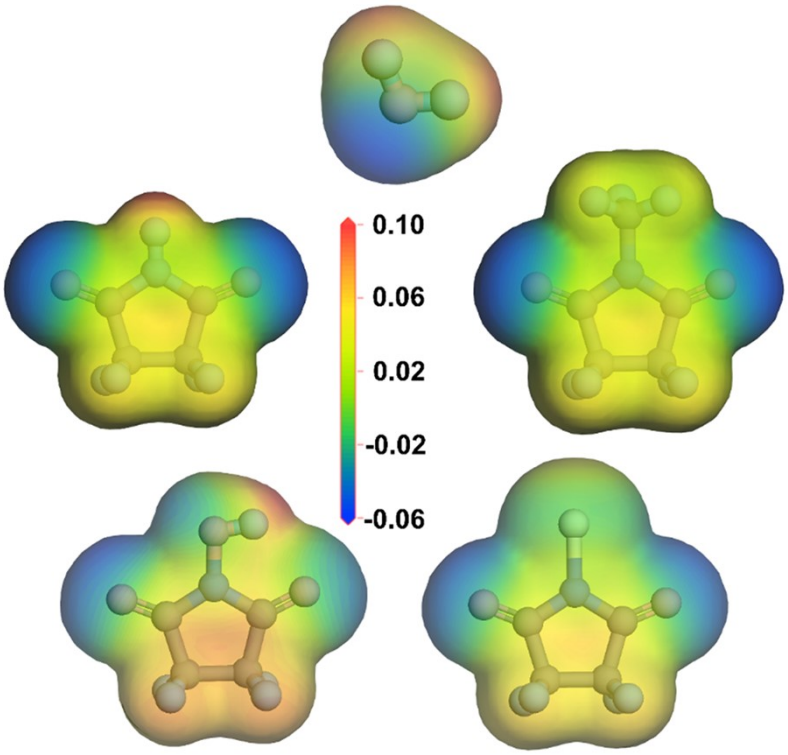

Fig. S6 ESP mapping of H_2O and x-SUs.

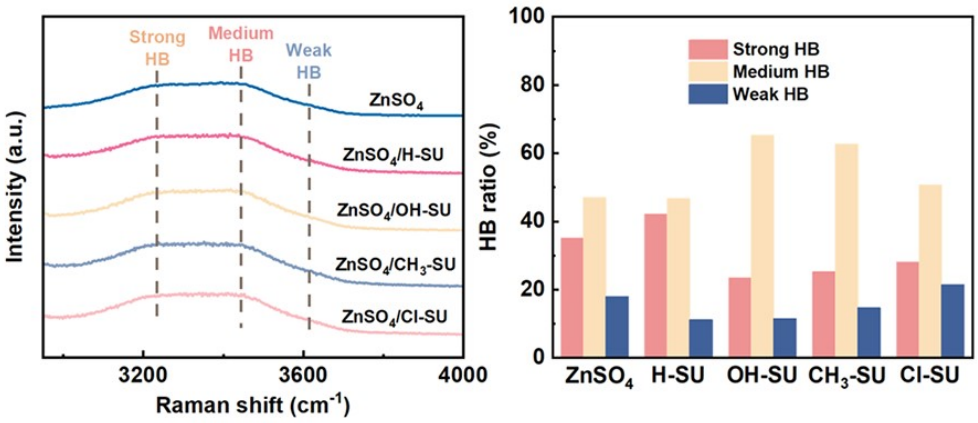

Fig. S7 Raman spectra of different electrolytes and related HB ratio.

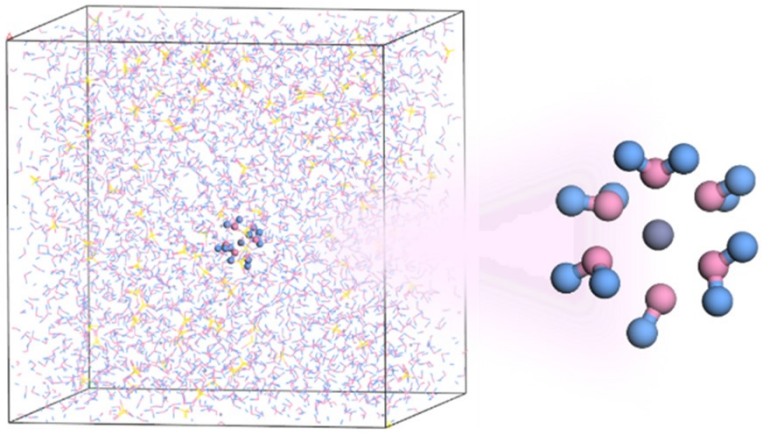

Fig. S8 3D snapshots of the MD simulations for $ZnSO_4$ and corresponding enlarged snapshots of Zn^{2+} solvation structure.

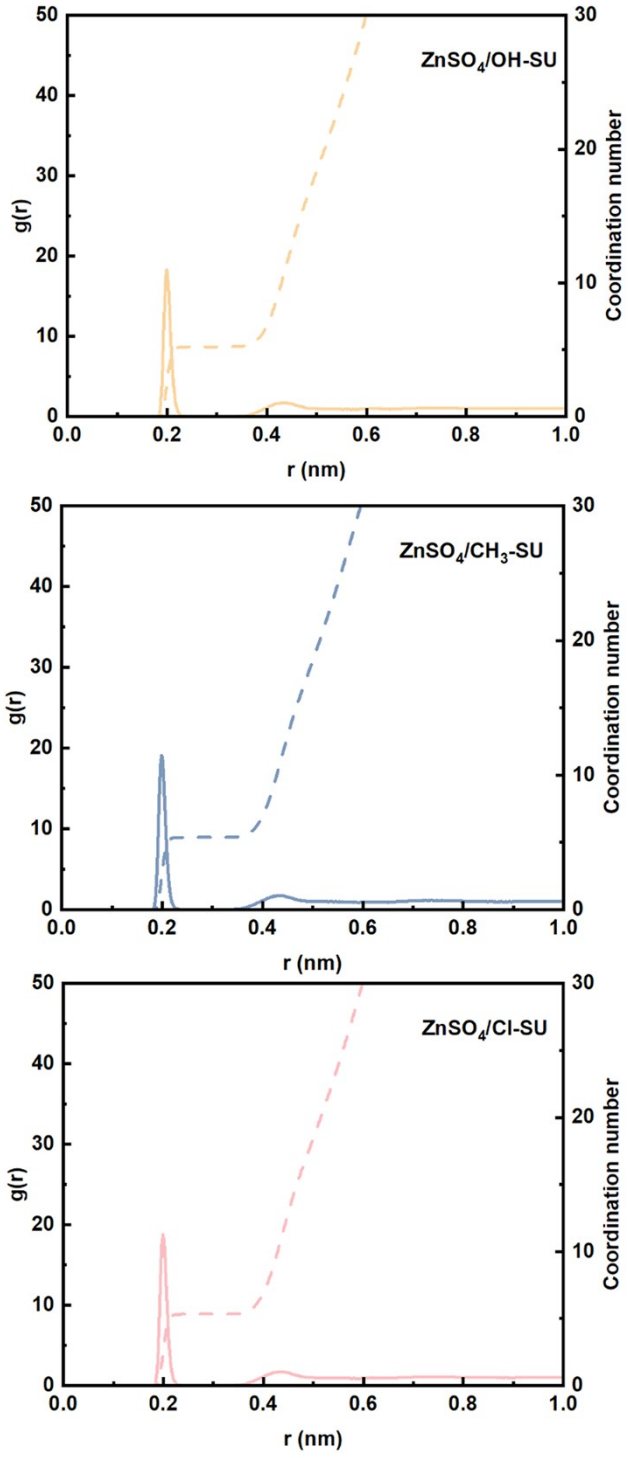

Fig. S9 Radial distribution functions and corresponding coordination numbers of Zn^{2+}-O (H_2O) in different electrolytes.

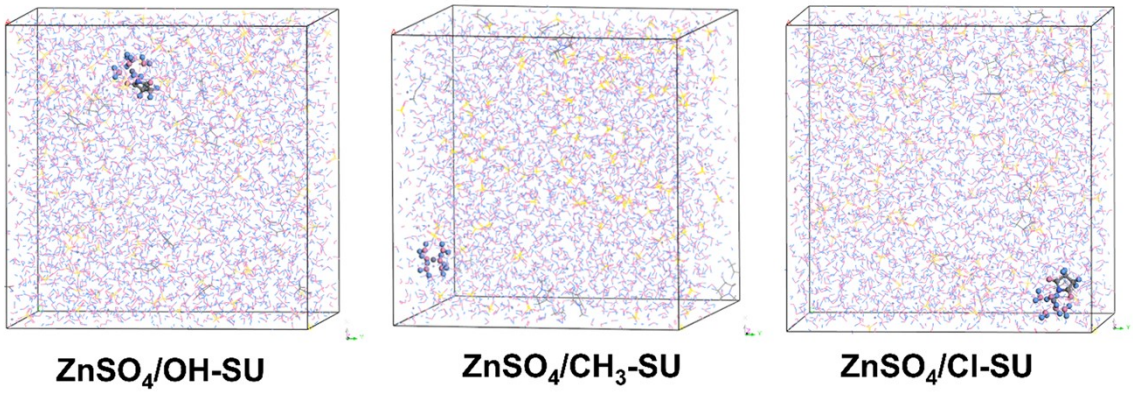

Fig. S10 3D snapshots of the MD simulations for ZnSO4/x-SUs

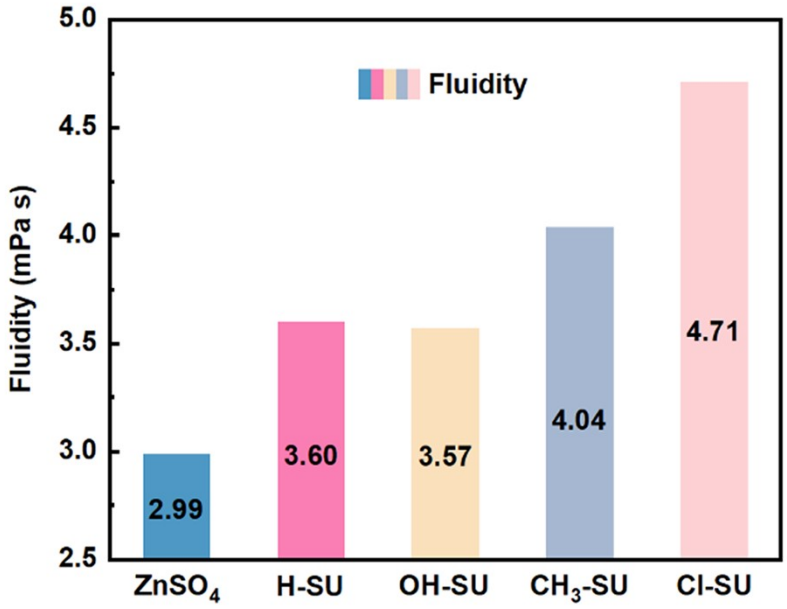

Fig. S11 Viscosity of different electrolytes.

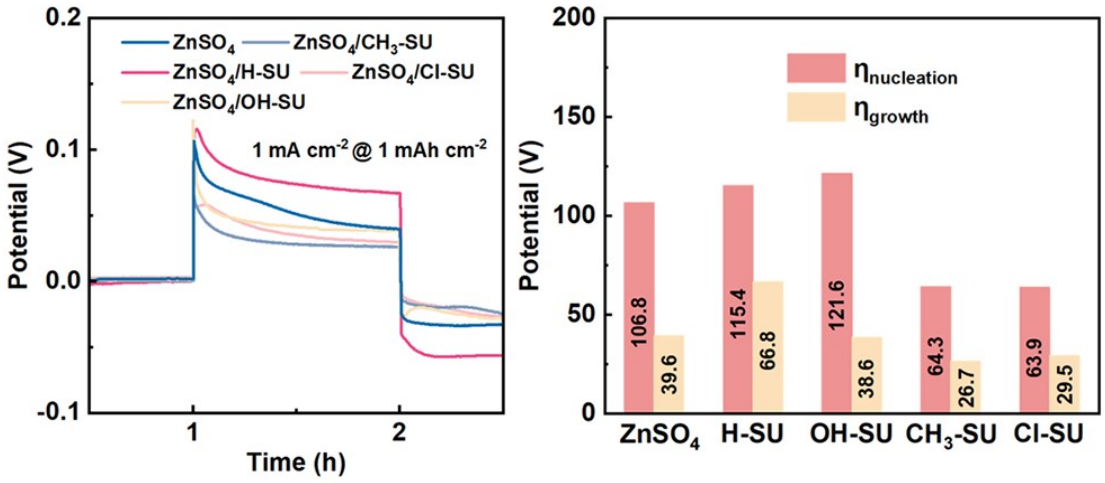

Fig. S12 The $\eta_{nucleation}$ and η_{growth} of the initial Zn plating.

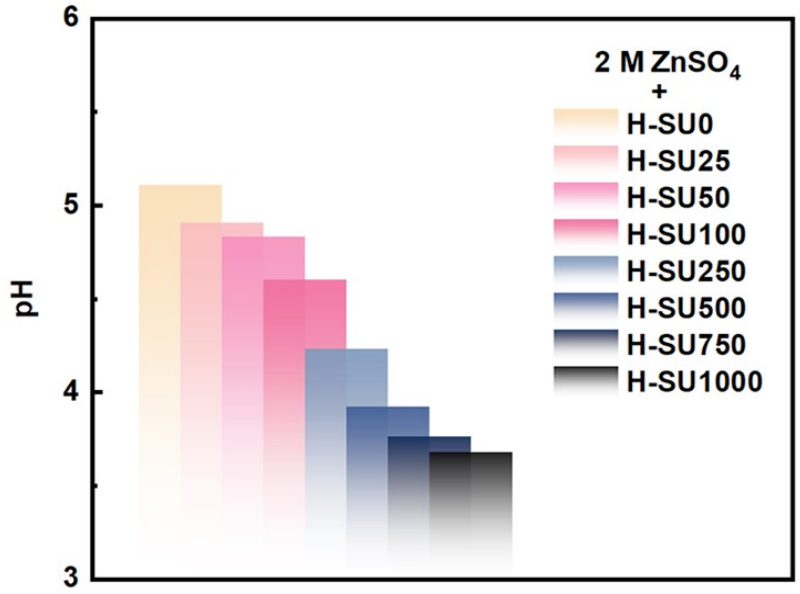

Fig. S13 pH value of $ZnSO_4$ with different concentration of H-SU.

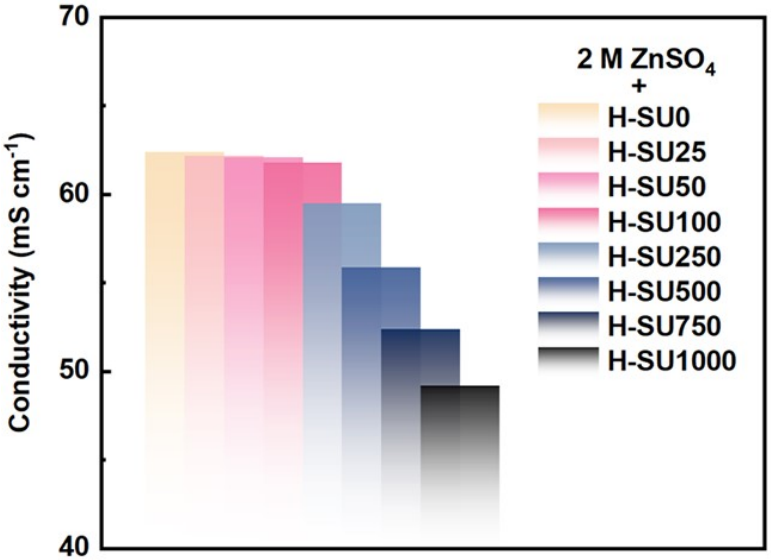

Fig. S14 Ionic conductivity of $ZnSO_4$ with different concentrations of H-SU.

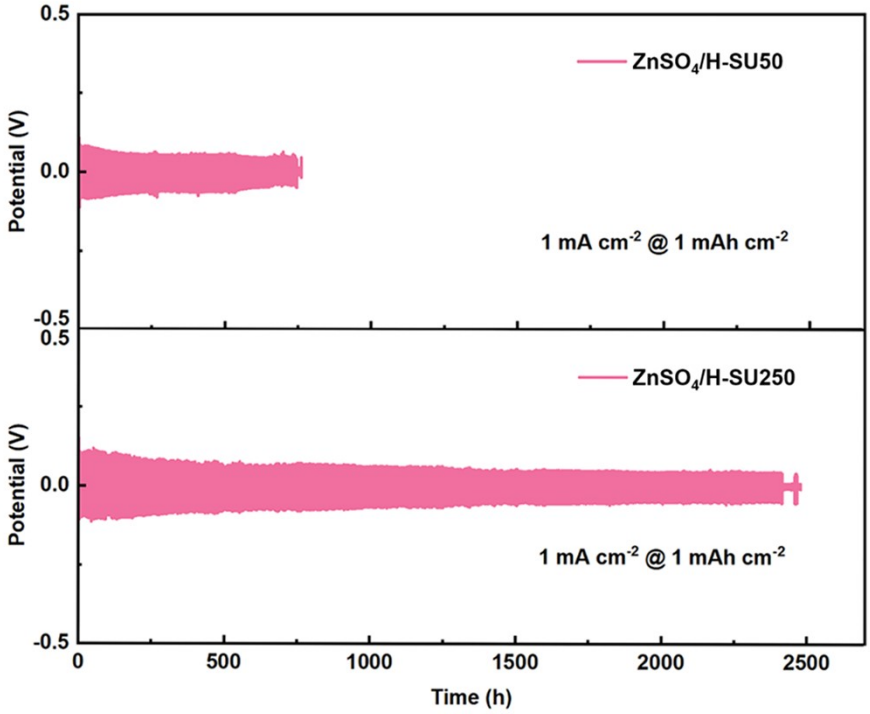

Fig. S15 Cycling performance of Zn||Zn symmetric cells in $ZnSO_4$ with different concentrations of H-SU at 1 mA cm^{-2} @ 1 mAh cm^{-2}.

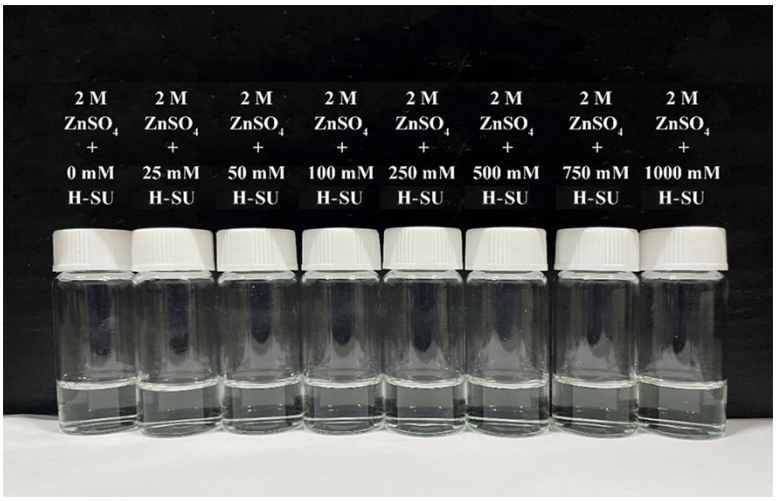

Fig. S16 The physical state of $ZnSO_4$ with different concentrations of H-SU.

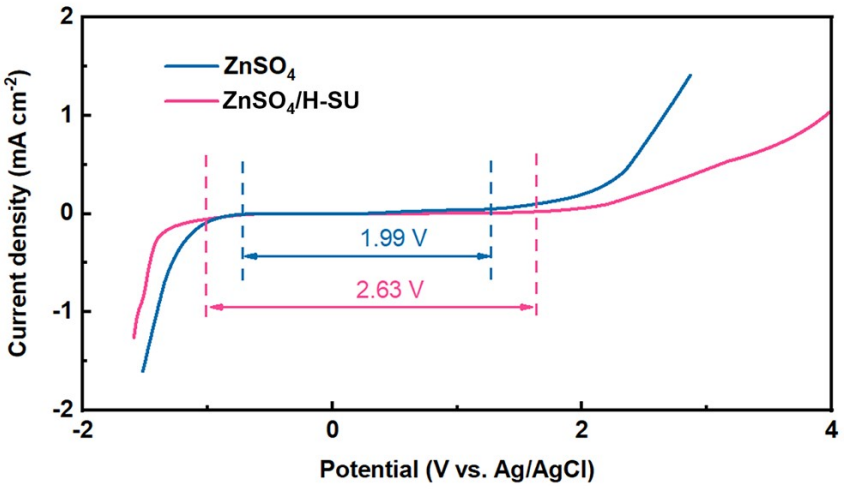

Fig. S17 Electrochemical stability window of $ZnSO_4$ and $ZnSO_4$/H-SU.

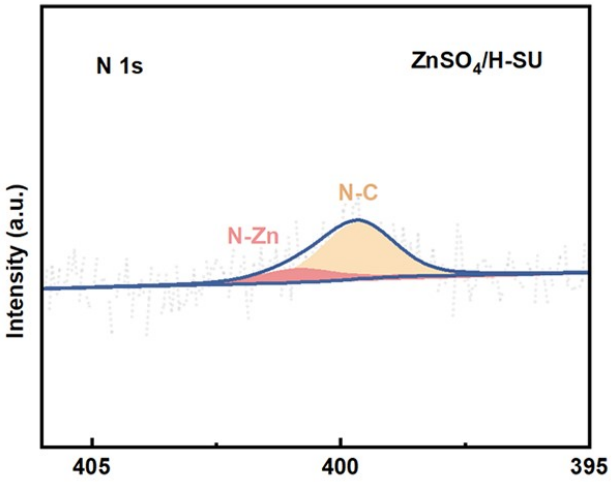

Fig. S18 N1s XPS spectra of Zn cycled in $ZnSO_4$/H-SU.

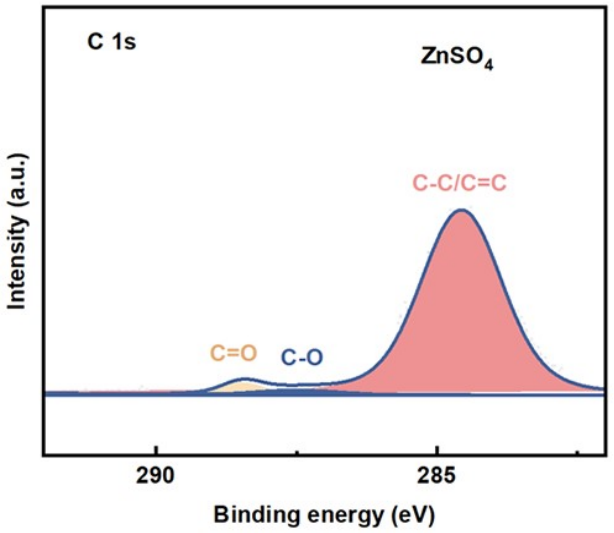

Fig. S19 C1s XPS spectra of Zn cycled in pristine $ZnSO_4$.

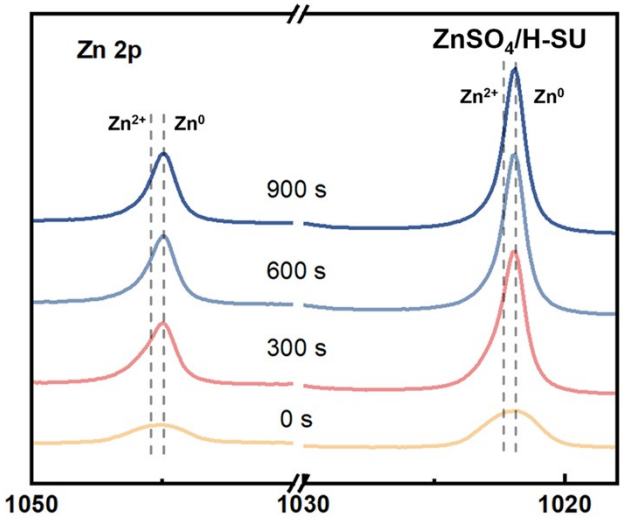

Fig. S20 In-depth Zn2p XPS spectra of $ZnSO_4$/H-SU.

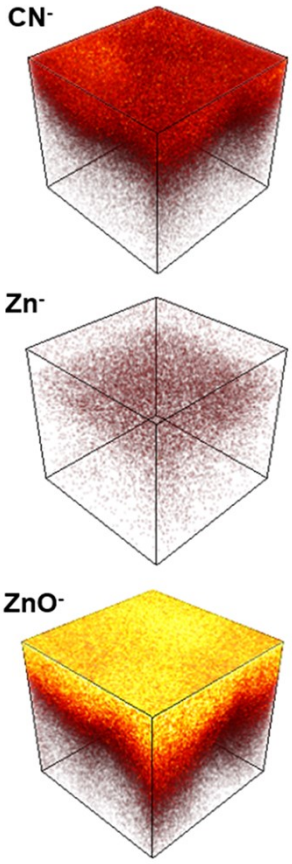

Fig. S21 3D TOF-SIMS images of Zn after 20 cycles in $ZnSO_4$/H-SU.

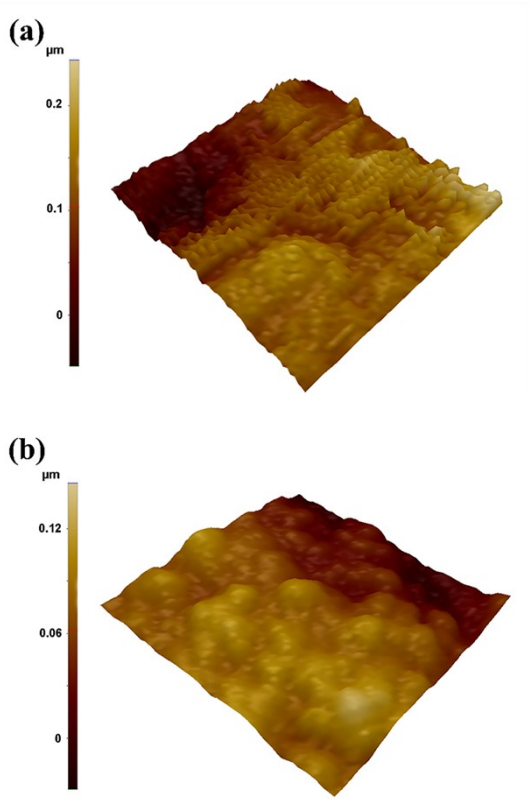

Fig. S22 AFM images of Zn after 20 cycles in a) $ZnSO_4$ and b) $ZnSO_4$/H-SU.

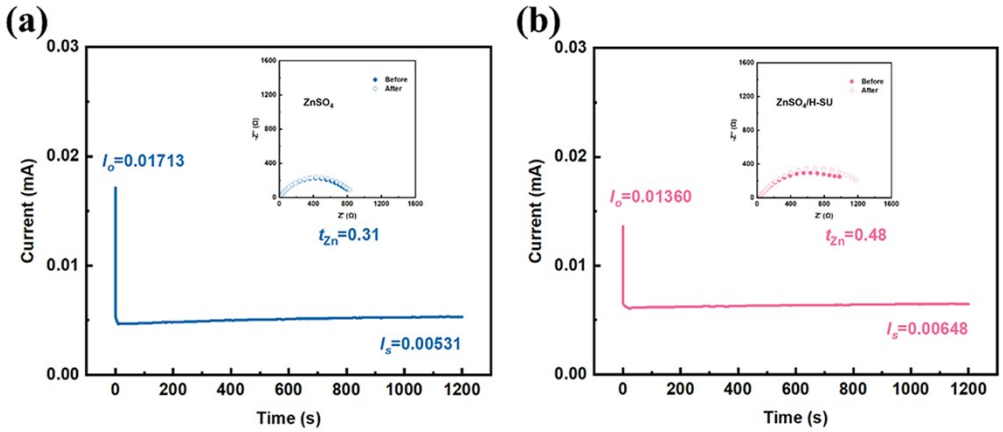

Fig. S23 Transference number of Zn^{2+} in a) $ZnSO_4$ and b) $ZnSO_4$/H-SU.

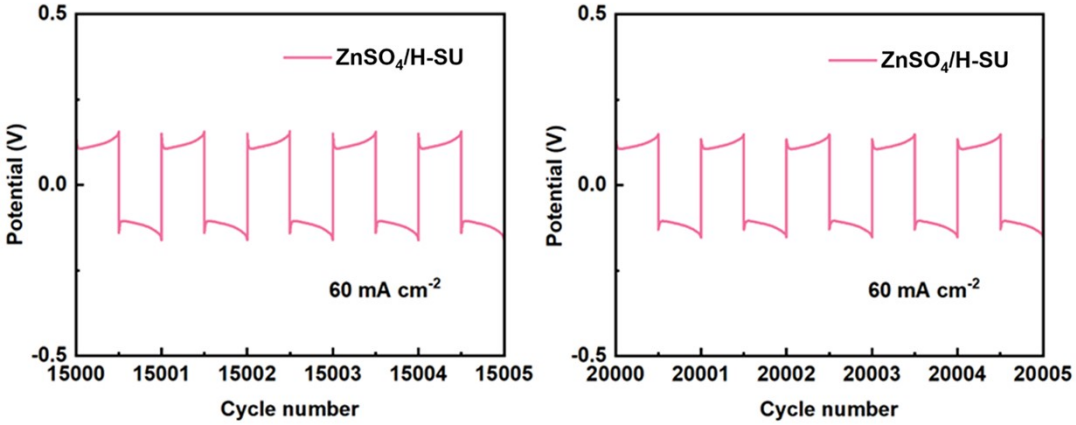

Fig. S24 Enlarged images of Fig. 4b for cycle numbers 15000-15005 and 20000-20005.

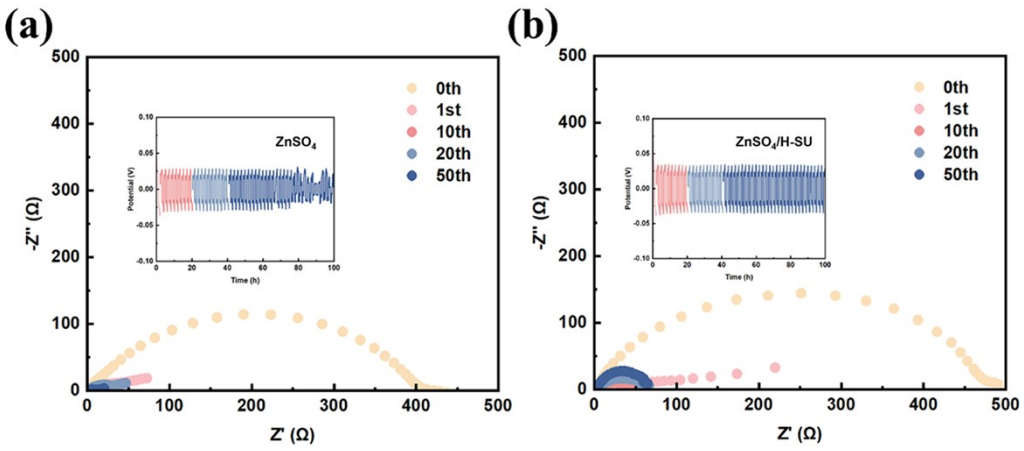

Fig. S25 In-situ EIS spectra of a) $ZnSO_4$ and b) $ZnSO_4$/H-SU.

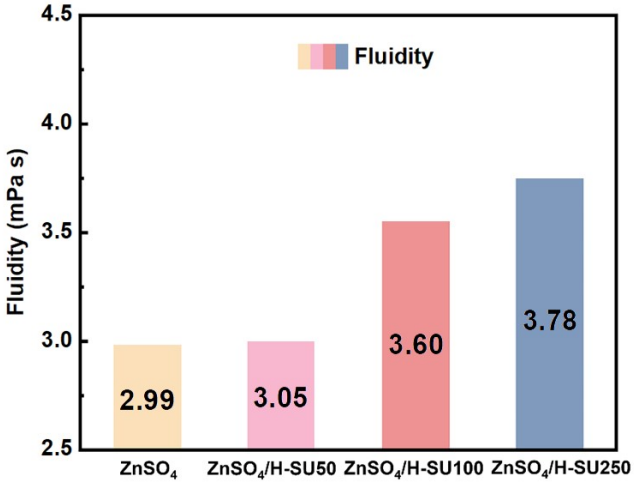

Fig. S26 Fluidity of $ZnSO_4$ with different concentrations of H-SU.

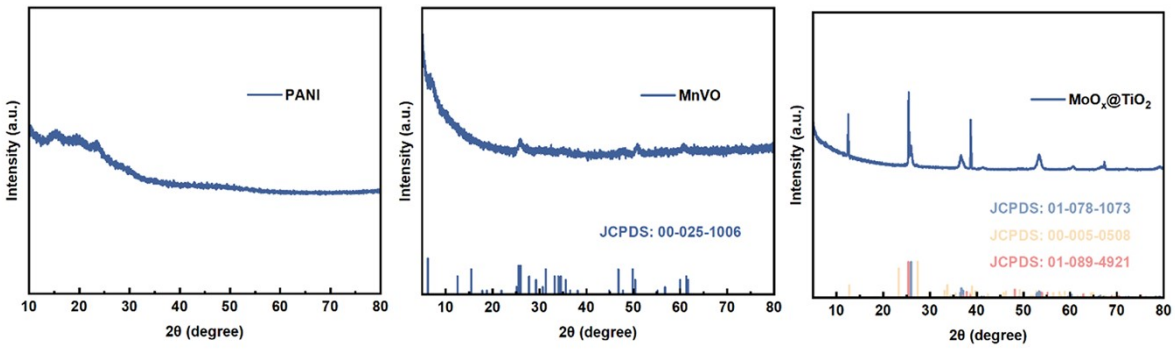

Fig. S27 XRD spectra of three cathodes.

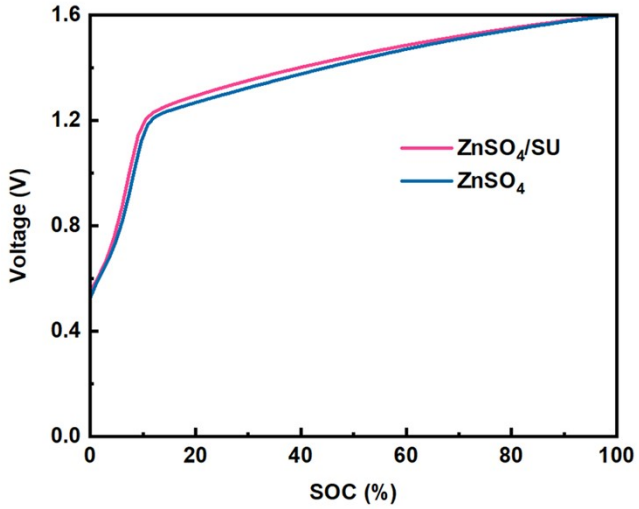

Fig. S28 Initial charge curves of SS||PANI. This figure confirms that the PANI cathode in this work does not store the additive anion.

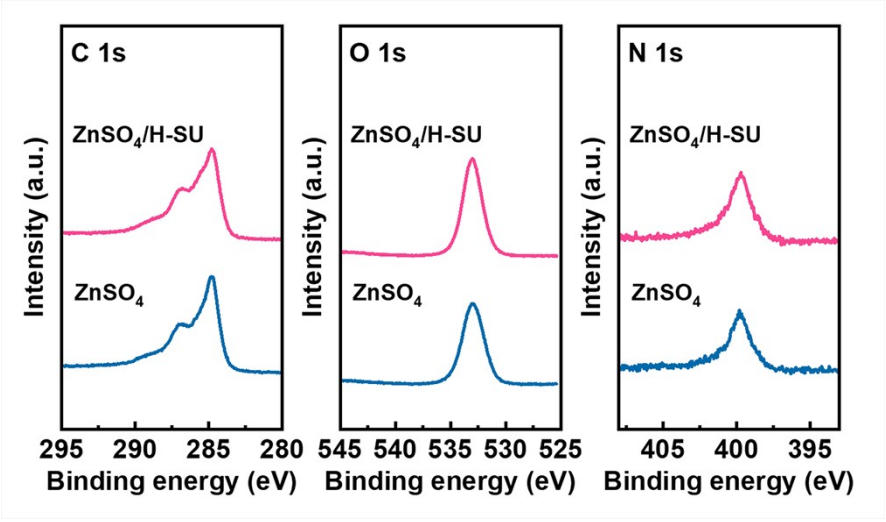

Fig. S29 XPS spectra of PANI charged to 1.6 V in different electrolytes.

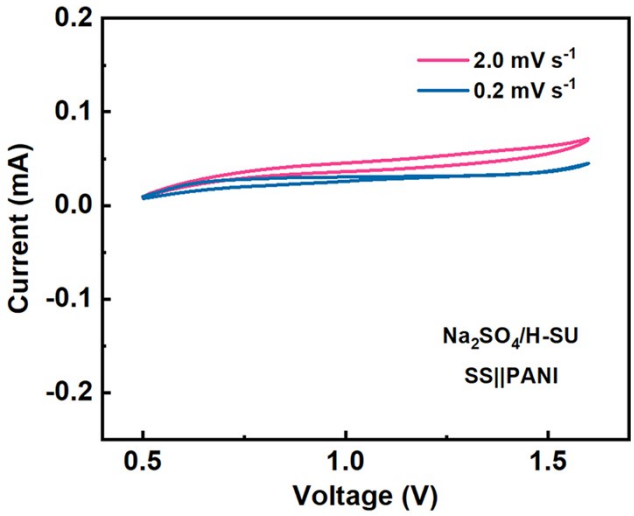

Fig. S30 CV curves of SS||PANI in Na_2SO_4/H-SU. This figure demonstrates that SO_4^{2-} and H-SU do not participate in anion storage.

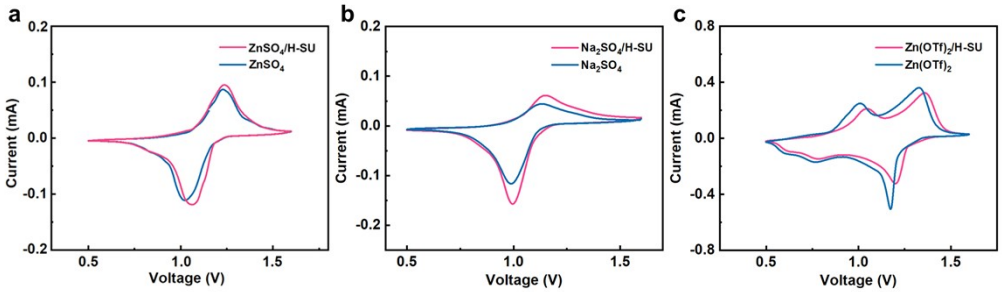

Fig. S31 CV curves of Zn||PANI in a) $ZnSO_4$, $ZnSO_4$/H-SU, b) Na_2SO_4, Na_2SO_4/H-SU, c) $Zn(OTf)_2$ and $Zn(OTf)_2$/H-SU for 2nd cycle. Regardless of the salt, the additive does not participate in storage. Importantly, by comparing the peak positions in the figures, we confirmed that the working mechanism of PANI in our study is based on Zn^{2+} storage, not anion storage.

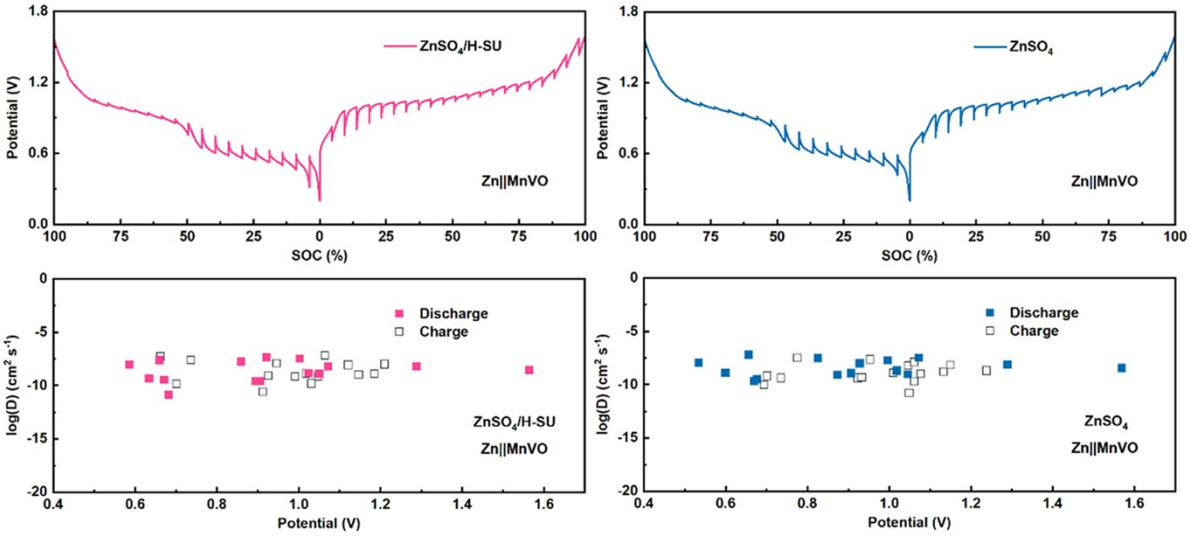

Fig. S32 GITT curves of Zn||MnVO and the corresponding calculated diffusion coefficients. This figure confirms that the MnVO cathode primarily operates based on Zn^{2+} storage, and the presence of H-SU does not alter this mechanism.

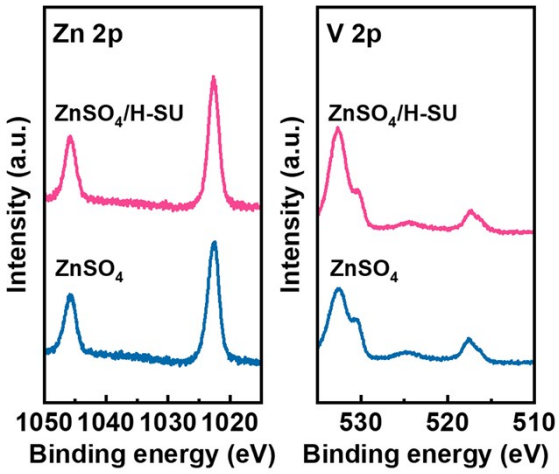

Fig. S33 XPS spectra of MnVO discharged to 0.2 V in different electrolytes.

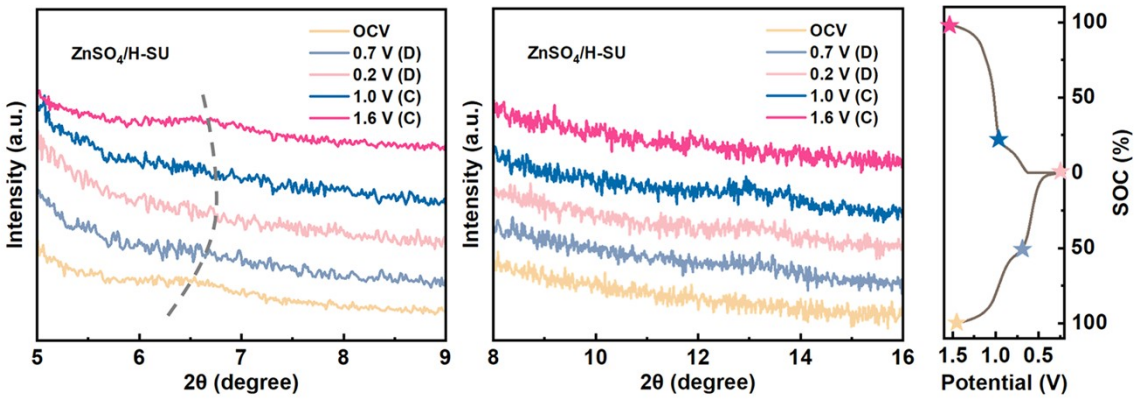

Fig. S34 Ex-situ xrd spectra of MnVO in $ZnSO_4$/H-SU.

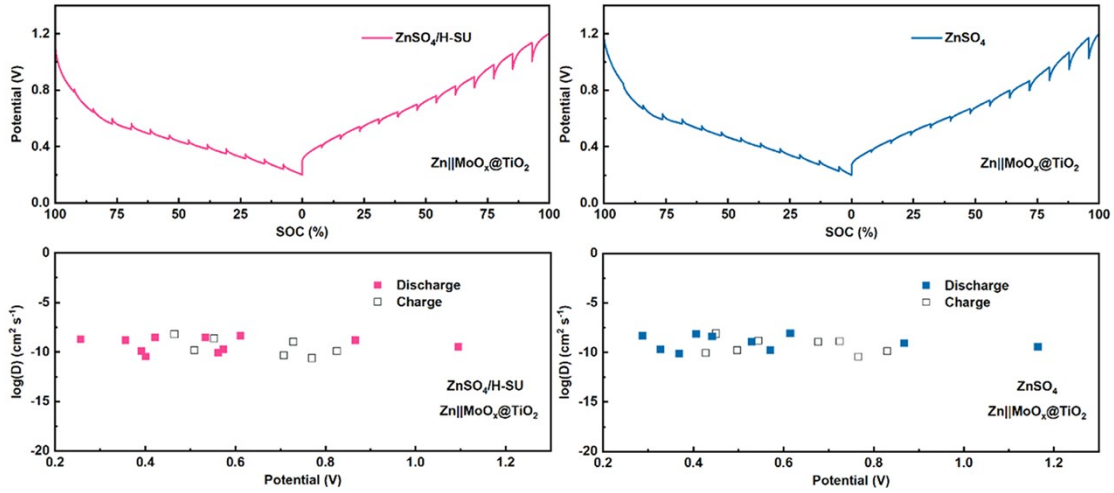

Fig. S35 GITT curves of Zn||MoO_x@TiO_2 and the corresponding calculated diffusion coefficients. This figure confirms that the MoO_x@TiO_2 cathode primarily operates based on Zn^{2+} storage.

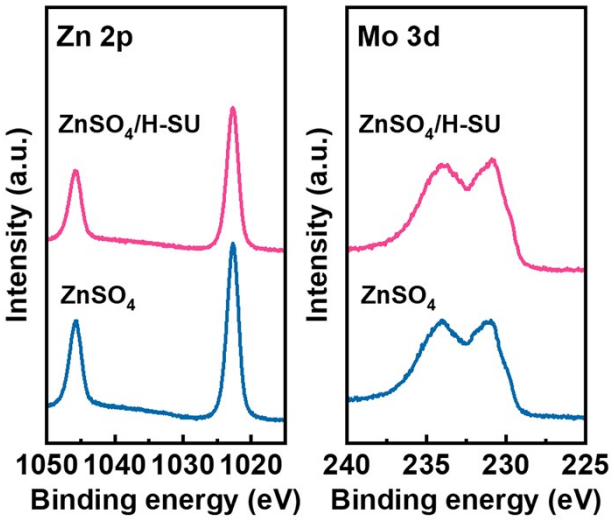

Fig. R36 XPS spectra of MoO_x@TiO_2 discharged to 0.2 V in different electrolytes.

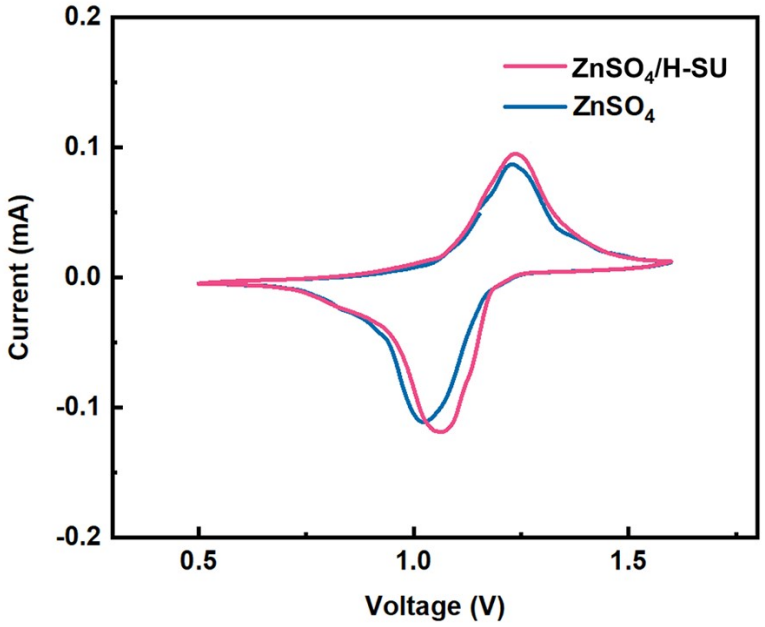

Fig. S37 CV curves of Zn||PANI in different electrolytes.

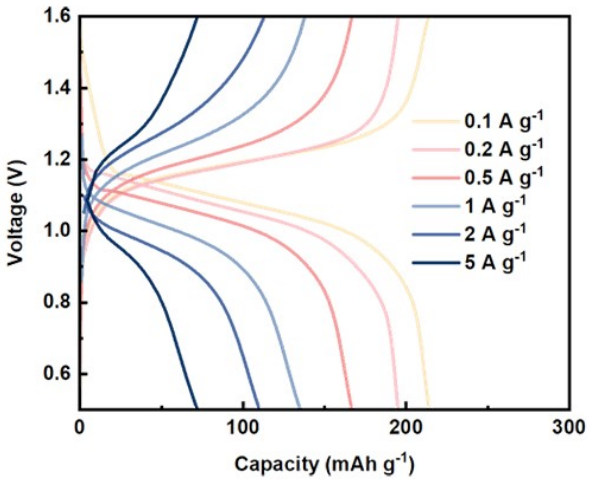

Fig. S38 Galvanostatic charge-discharge profiles of Zn||PANI in $ZnSO_4$/H-SU at various current densities.

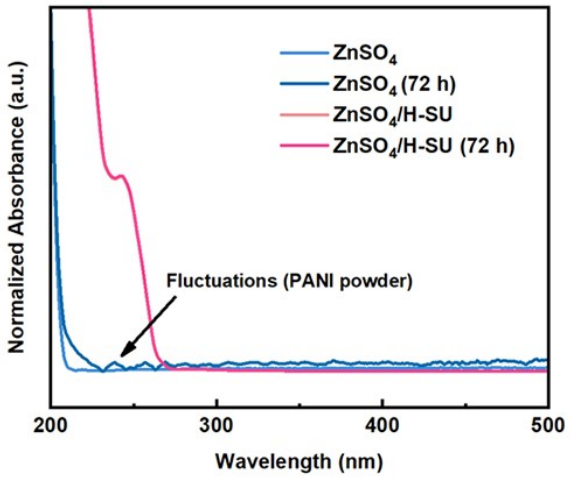

Fig. S39 UV-vis spectra of different electrolytes before/after immersing PANI cathodes for 72 h.

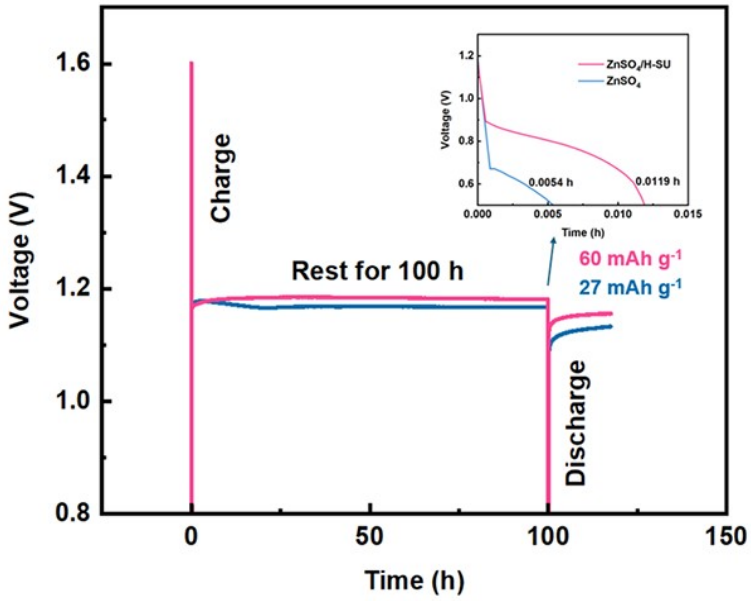

Fig. S40 Self-discharge curves of different electrolytes.

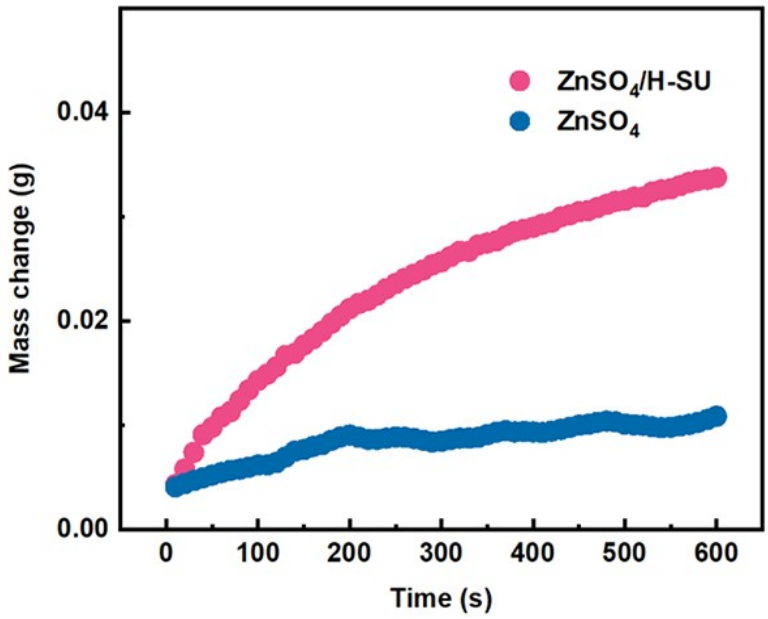

Fig. S41 m-t curve from wetting balance test.

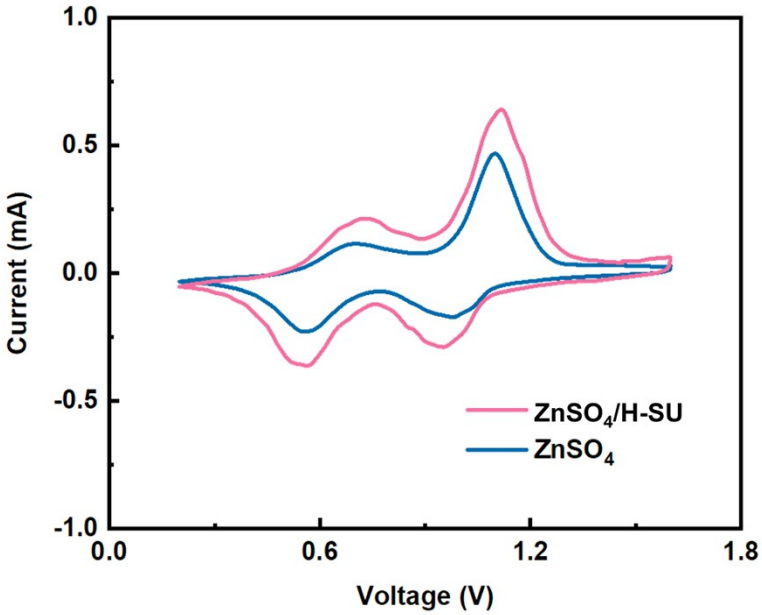

Fig. S41 CV curves of Zn||MnVO in different electrolytes.

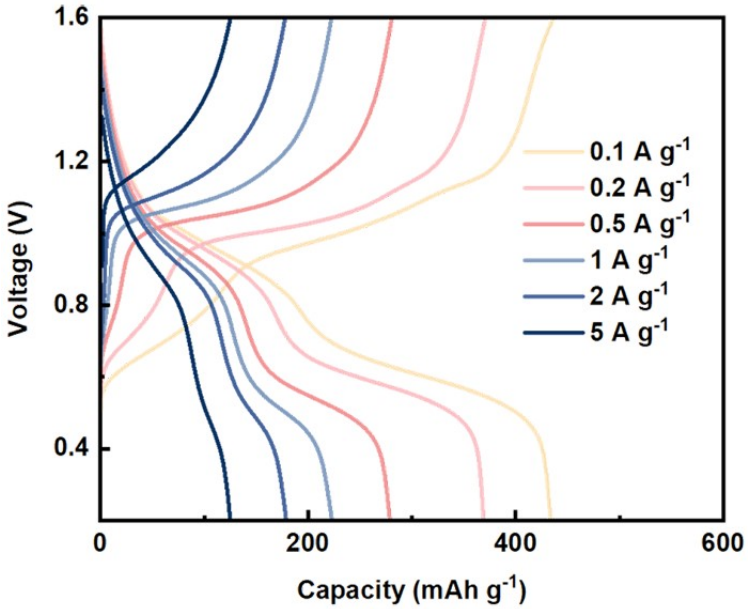

Fig. S43 Galvanostatic charge-discharge profiles of Zn||MnVO in $ZnSO_4$/H-SU at various current densities.

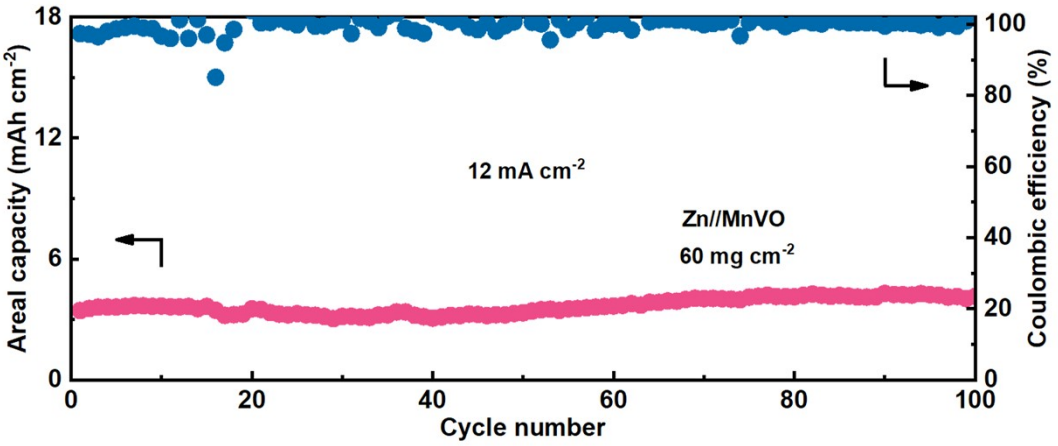

Fig. S44 Cycling performance of Zn||MnVO cells with a ultra-high loading MnVO in $ZnSO_4$/H-SU at 12 mA cm^{-2}.

Fig. S45 Zn||MnVO pouch cell-powered electronic alarm clock.

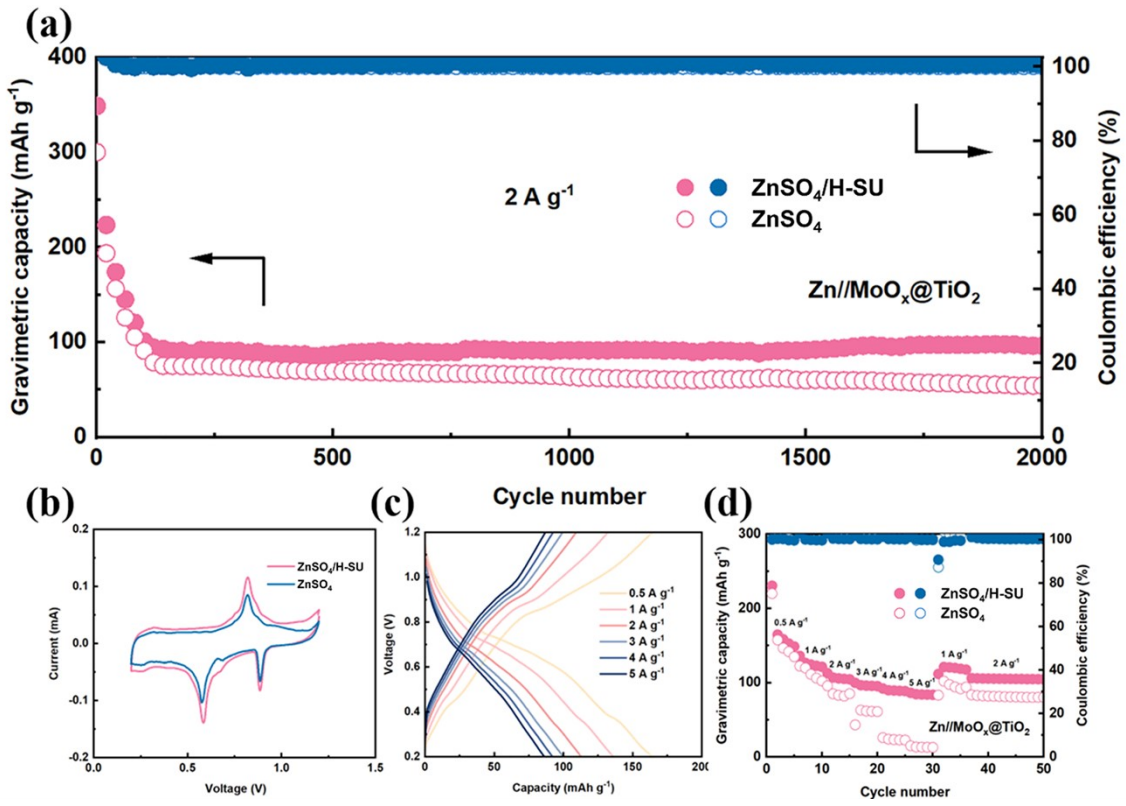

Fig. S46 a) Cycling performance of Zn||MoO_x@TiO_2 in different electrolytes at 2 A g^{-1}. b) CV curves of Zn||MoO_x@TiO_2 in different electrolytes. c) Galvanostatic charge-discharge profiles of Zn||MoO_x@TiO_2 in $ZnSO_4$/H-SU. d) Rate performance of Zn||MoO_x@TiO_2 in different electrolytes.

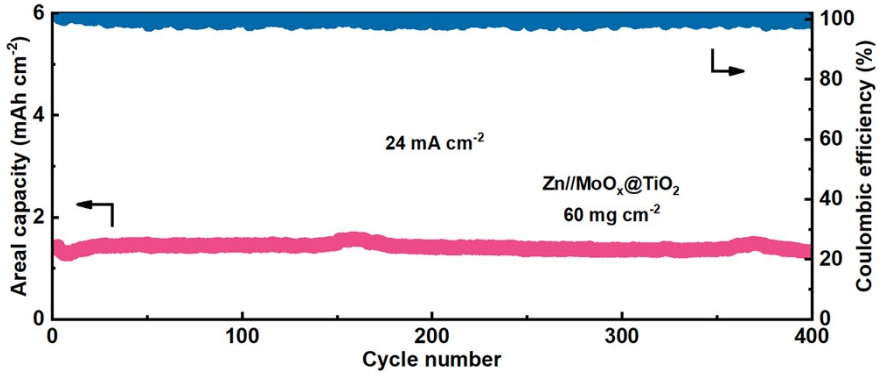

Fig. S47 Cycling performance of ultra-high loading Zn||MoO_x@TiO_2 cells in $ZnSO_4$/H-SU at 24 mA cm^{-2}.

Table S1 Comparison of imide additives.

Product	Formula	Chemical structure	Price (1 kg)
H-SU	**$C_4H_5NO_2$**		**$45.00**
OH-SU	$C_4H_5NO_3$		$50.00
CH_3-SU	$C_5H_7NO_2$		$2201.80
Cl-SU	$C_4H_4ClNO_2$		$55.00
Diacetamide	$C_4H_7NO_2$	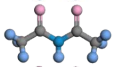	$10240.00
N-hydroxydiacetamide	$C_4H_7NO_3$	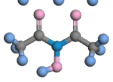	$47600.00
N-methyldiacetamide	$C_5H_9NO_2$	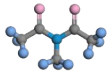	$6580.00
N-chlorodiacetamide	$C_4H_6ClNO_2$	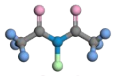	Not commercial
N-(2-chloroacetyl)acetamide	$C_4H_6ClNO_2$	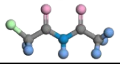	$233684.00

The data is sourced from www.chemicalbook.com.

Table S2. Fukui function results of N and LUMO-HOMO isosurfaces.

	Fukui f^0 (a. u.)	**LUMO (eV)**	**HOMO (eV)**
H_2O	/	0.0313	-0.2457
H-SU	0.019	-0.0656	-0.2222
OH-SU	0.017	-0.0753	-0.2329
CH_3-SU	0.002	-0.0602	-0.2187
Cl-SU	0.013	-0.0914	-0.2350

Table S3. Corresponding coordination numbers of primary solvation structure in different electrolytes.

	$ZnSO_4$	**$ZnSO_4$/H-SU**	**$ZnSO_4$/OH-SU**	**$ZnSO_4$/CH_3-SU**	**$ZnSO_4$/Cl-SU**
Zn^{2+}-O (H_2O)	5.66	5.20	5.23	5.37	5.32

Table S4. Comparison of cyclic reversibility using aqueous electrolyte strategies in recent reports.

Electrolyte	Current density @ Capacity	Cycle number	Ref.
2 M $ZnSO_4$ + 50 mM NH_4OAc	10 mA cm^{-2} @ 1 mAh cm^{-2}	1000	[1]
1 M $ZnSO_4$ + 15 mM Co(TAPC)	50 mA cm^{-2} @ 1 mAh cm^{-2}	8000	[2]
2 M $ZnSO_4$ + 1 mM HEDP	10 mA cm^{-2} @ 1 mAh cm^{-2}	1435	[3]
3 M $ZnSO_4$ + 5% TD	10 mA cm^{-2} @ 2 mAh cm^{-2}	600	[4]
1 M $ZnSO_4$ + 500 mM Na_2SO_4 + 1 g L^{-1} PAM	20 mA cm^{-2} @ 1 mAh cm^{-2}	1100	[5]
1 M $ZnSO_4$ + 5 mM Thiourea	10 mA cm^{-2} @ 1 mAh cm^{-2}	3000	[6]
2 M $ZnSO_4$ + 0.01 g L^{-1} NSQD	20 mA cm^{-2} @ 1 mAh cm^{-2}	~6000	[7]
2 M $ZnSO_4$ + 0.05 mM TBA_2SO_4	10 mA cm^{-2} @ 2 mAh cm^{-2}	1000	[8]
4 M@CMC|1 M|4 M@CMC ($ZnSO_4$)	20 mA cm^{-2} @ 1 mAh cm^{-2}	>10000	[9]
1 M $Zn(BBI)_2$	20 mA cm^{-2} @ 1 mAh cm^{-2}	7000	[10]
1 M $ZnSO_4$ + 6 mM $(NH_4)_6[Mo_7O_{24}]\cdot 4H_2O$	10 mA cm^{-2} @ 1 mAh cm^{-2}	568	[11]
1 M $ZnSO_4$ + 0.14 g L^{-1} nano-Si	10 mA cm^{-2} @ 2 mAh cm^{-2}	298	[12]
2 M $ZnSO_4$ + 0.44 mM Irgacure 2959	10 mA cm^{-2} @ 5 mAh cm^{-2}	~200	[13]
4 M $Zn(OTf)_2$ + 250 mM Tetramethylurea	5 mA cm^{-2} @ 2.5 mAh cm^{-2}	>1600	[14]
2 M $ZnSO_4$ + 5 g L^{-1} silk peptide	5 mA cm^{-2} @ 1 mAh cm^{-2}	2250	[15]
2 M $ZnSO_4$ in H_2O/DMF (4:2 in volume ratio)	4 mA cm^{-2} @ 1 mAh cm^{-2}	2000	[16]
2 M $ZnSO_4$ + 100 mM $MgSO_4$	1 mA cm^{-2} @ 0.25 mAh cm^{-2}	1200	[17]
1 M $Zn(ClO_4)_2$ + 10 mM β-CD	1 mA cm^{-2} @ 1 mAh cm^{-2}	500	[18]
2 M $ZnSO_4$ + 0.5 g L^{-1} C_3N_4 QDs	1 mA cm^{-2} @ 1 mAh cm^{-2}	600	[19]
2 M $ZnSO_4$ + 8.5 M $La(NO_3)_3$	1 mA cm^{-2} @ 1 mAh cm^{-2}	600	[20]
2 M $ZnSO_4$ + 100 mM H-SU	**60 mA cm^{-2} @ 1 mAh cm^{-2}**	**>21000**	**This work**

Table S5 Comparison of Zn||PANI batteries with recently published works claiming low N/P ratios or high mass loading.

Method	n/p ratio	Mass loading (mg cm^{-2})	Areal current density (mA cm^{-2})	Areal capacity (mAh cm^{-2})	Ref.
H-SU additive	**2.2**	**60**	**6**	**4.2**	**This work**
PMCNA additive	2.6	20	4	1.67	[21]
TPAS additive	4.48	10.96	10.96	0.67	[22]
Con-CMC	3.3	9	9	~0.24	[23]
ZIL in EG/H_2O	2.5	3	1.5	0.2	[24]
TFMP additive	5.4	9	0.36	1.08	[25]
PCA-Zn additive	4.4	1.8	1.8	~0.09	[26]
AlOTf/ACN-HE	27.8	10	2	0.63	[27]
TEOA additive	4.2	23	11.5	~1.26	[28]

Table S6 Comparison of Zn||V-based batteries with recently published works claiming low N/P ratios or high mass loading.

Method	n/p ratio	Mass loading (mg cm^{-2})	Areal current density (mA cm^{-2})	Areal capacity (mAh cm^{-2})	Ref.
H-SU additive	**3.3**	**60**	**12**	**4.2**	**This work**
MVOH	3.61	12.3	6.15	>3	[29]
V_2O_5@LIG	9.72	17.1	17.1	6.05	[30]
NMP additive	~4.7	~5.5	19.25	~1.55	[31]
N,S-CDs additive	1.05	11.52	11.52	~2	[32]
PAPE@Zn	0.6	~17	17	2.33	[33]
3DGT@Zn	1.74	11.4	4	>2	[34]
SIA additive	4.2	9.2	0.46	~1.8	[35]
DMAC/TMP	/	6.6	3.3	~0.8	[36]

Table S7 Comparison of Zn||Mo-based batteries with recently published works.

Method	n/p ratio	Mass loading (mg cm^{-2})	Areal current density (mA cm^{-2})	Areal capacity (mAh cm^{-2})	Ref.
H-SU additive	**8.4**	**60**	**24**	**1.32**	**This work**
MoO_{3-x}@PPy	/	2	2	0.212	[37]
MoO_{3-x}	/	2	4	0.288	[38]
S-MoO_2	/	1.91	3.82	~0.24	[39]
MoS_2-CTAB	/	11.5	11.5	0.87	[40]
$MoTe_{1.7}$	/	5	5	1.19	[41]
MoO_2@NC	~577	1.5	7.5	0.065	[42]

References:

1. D. L. Han, Z. X. Wang, H. T. Lu, H. Li, C. J. Cui, Z. C. Zhang, R. Sun, C. N. Geng, Q. H. Liang, X. X. Guo, Y. B. Mo, X. Zhi, F. Y. Kang, Z. Weng and Q. H. Yang, *Adv Energy Mater*, 2022, **12**, 2102982**.**
2. K. P. Zhu, C. Guo, W. B. Gong, Q. H. Xiao, Y. G. Yao, K. Davey, Q. H. Wang, J. F. Mao, P. Xue and Z. P. Guo, *Energ Environ Sci*, 2023, **16**, 3612-3622.
3. M. Li, K. X. Xie, R. Y. Peng, B. Y. Yuan, Q. H. Wang and C. Wang, *Small*, 2022, **18**, 2107398.
4. K. Wang, T. Qiu, L. Lin, X. X. Liu and X. Q. Sun, *Energy Storage Mater*, 2023, **54**, 366-373.
5. Q. Zhang, J. Y. Luan, L. Fu, S. G. Wu, Y. G. Tang, X. B. Ji and H. Y. Wang, *Angew Chem Int Edit*, 2019, **58**, 15841-15847.
6. H. Y. Qin, W. Kuang, N. Hu, X. M. Zhong, D. Huang, F. Shen, Z. W. Wei, Y. P. Huang, J. Xu and H. B. He, *Adv Funct Mater*, 2022, **32**, 2206695.
7. F. F. Wang, H. T. Lu, H. B. Zhu, L. Wang, Z. H. Chen, C. P. Yang and Q. H. Yang, *Energy Storage Mater*, 2023, **58**, 215-221.
8. A. Bayaguud, X. Luo, Y. P. Fu and C. B. Zhu, *ACS Energy Lett*, 2020, **5**, 3012-3020.
9. H. F. Lu, D. Zhang, Q. Z. Jin, Z. L. Zhang, N. Lyu, Z. J. Zhu, C. X. Duan, Y. Qin and Y. Jin, *Adv Mater*, 2023, **35**, 2300620.
10. H. R. Du, Y. H. Dong, Q. J. Li, R. R. Zhao, X. Q. Qi, W. H. Kan, L. M. Suo, L. Qie, J. Li and Y. H. Huang, *Adv Mater*, 2023, **35**, 2210055.
11. H. Y. Wu, X. X. Gu, P. Huang, C. Sun, H. Hu, Y. Zhong and C. Lai, *J Mater Chem A*, 2021, **9**, 7025-7033.
12. H. Y. Wu, W. Yan, Y. M. Xing, L. Li, J. Y. Liu, L. Li, P. Huang, C. Lai, C. Wang, W. H. Chen and S. L. Chou, *Adv Funct Mater*, 2024, **34**, 2213882.
13. T. C. Li, C. J. Lin, M. Luo, P. J. Wang, D. S. Li, S. Z. Li, J. Zhou and H. Y. Yang, *ACS Energy Lett*, 2023, **8**, 3258-3268.
14. J. H. Yang, Y. Zhang, Z. L. Li, X. Xu, X. Y. Su, J. W. Lai, Y. Liu, K. Ding, L. Y. Chen, Y. P. Cai and Q. F. Zheng, *Adv Funct Mater*, 2022, **32**, 2209642.
15. B. J. Wang, R. Zheng, W. Yang, X. Han, C. Y. Hou, Q. H. Zhang, Y. G. Li, K. R. Li and H. Z. Wang, *Adv Funct Mater*, 2022, **32**, 2112693.
16. P. X. Xiong, Y. B. Kang, N. Yao, X. Chen, H. Y. Mao, W. S. Jang, D. M. Halat, Z. H. Fu, M. H. Jung, H. Y. Jeong, Y. M. Kim, J. A. Reimer, Q. Zhang and H. S. Park, *ACS Energy Lett*, 2023, **8**, 1613-1625.
17. P. J. Wang, X. S. Xie, Z. Y. Xing, X. H. Chen, G. Z. Fang, B. A. Lu, J. Zhou, S. Q. Liang and H. J. Fan, *Adv Energy Mater*, 2021, **11**, 2101158.
18. M. J. Qiu, P. Sun, Y. Wang, L. Ma, C. Y. Zhi and W. J. Mai, *Angew Chem Int Edit*, 2022, **61**, e202210979.
19. W. Y. Zhang, M. Y. Dong, K. R. Jiang, D. L. Yang, X. H. Tan, S. L. Zhai, R. F. Feng, N. Chen, G. King, H. Zhang, H. B. Zeng, H. Li, M. Antonietti and Z. Li, *Nat Commun*, 2022, **13**, 5348.
20. R. R. Zhao, H. F. Wang, H. R. Du, Y. Yang, Z. H. Gao, L. Qie and Y. H. Huang, *Nat Commun*, 2022, **13**, 3252.
21. D. D. Feng, Y. C. Jiao and P. Y. Wu, *Angew Chem Int Edit*, 2023, **135**, e202314456.
22. L. Qian, H. J. Zhu, T. T. Qin, R. Yao, J. W. Zhao, F. Y. Kang and C. Yang, *Adv Funct Mater*, 2023, **33**, 2301118.
23. Y. H. Quan, H. Ma, M. F. Chen, W. J. Zhou, Q. H. Tian, X. Han and J. Z. Chen, *ACS Appl Mater Inter*, 2023, **15**, 44974-44983.
24. M. Y. Zhong, Y. Wang, Y. H. Xie, S. Y. Yuan, K. Ding, E. J. Begin, Y. J. Zhang, J. L. Bao and Y. G. Wang, *Adv*

Funct Mater, 2024, 2316788.

25. L. Ma, T. P. Pollard, M. A. Schroeder, C. Luo, Y. Zhang, G. Pastel, L. S. Cao, J. X. Zhang, V. Shipitsyn, Y. Yao, C. S. Wang, O. Borodin and K. Xu, *Energ Environ Sci*, 2024, **17**, 2468-2479.
26. S. Q. Jiao, J. M. Fu, Q. F. Yin, H. M. Yao and H. B. Hu, *Energy Storage Mater*, 2023, **59**, 102774.
27. Q. Y. Dou, N. Yao, W. K. Pang, Y. Park, P. X. Xiong, X. T. Han, H. H. Rana, X. Chen, Z. H. Fu, L. Thomsen, B. Cowie, Y. B. Kang, Q. Liu, D. H. Min, Y. M. Jung, Z. P. Guo, Q. Zhang and H. S. Park, *Energ Environ Sci*, 2022, **15**, 4572-4583.
28. W. J. Ge, H. L. Peng, J. J. Dong, G. L. Wang, L. F. Cui, W. Sun, X. J. Ma and J. Yang, *Chem Commun*, 2024, **60**, 750-753.
29. L. Yang, Y. J. Zhu, F. L. Zeng, L. Y. Dong, J. C. Tao, G. He and H. Li, *Energy Storage Mater*, 2024, **65**, 103162.
30. Z. Bie, Z. Y. Jiao, X. X. Cai, Z. T. Wang, X. Y. Zhang, Y. R. Li and W. X. Song, *Adv Energy Mater*, 2024, **14**, 2401002.
31. K. Wang, F. M. Liu, Q. R. Li, J. Q. Zhu, T. Qiu, X. X. Liu and X. Q. Sun, *Chem Eng J*, 2023, **452**, 139577.
32. Z. Xu, H. Li, Y. P. Liu, K. X. Wang, H. B. Wang, M. Z. Ge, J. P. Xie, J. L. Li, Z. R. Wen, H. Pan, S. N. Qu, J. L. Liu, Y. Y. Zhang, Y. X. Tang and S. Chen, *Mater Horiz*, 2023, **10**, 3680-3693.
33. J. Feng, X. Y. Li, Y. X. Ouyang, H. Y. Zhao, N. Li, K. Xi, J. Y. Liang and S. J. Ding, *Angew Chem Int Edit*, 2024, e202407194.
34. B. K. Wu, B. B. Guo, Y. Z. Chen, Y. B. Mu, H. Q. Qu, M. Lin, J. M. Bai, T. S. Zhao and L. Zeng, *Energy Storage Mater*, 2023, **54**, 75-84.
35. K. Q. Feng, B. C. Chen, B. J. Xi, C. X. Tian, B. Y. Sang, S. H. Meng, Y. Y. He, T. T. Gao, X. G. An, G. W. Zhou, S. L. Xiong and X. Wang, *Adv Energy Mater*, 2024, **14**, 2401053.
36. Y. Y. Wang, Z. J. Wang, W. K. Pang, W. Lie, J. A. Yuwono, G. M. Liang, S. L. Liu, A. M. D' Angelo, J. J. Deng, Y. M. Fan, K. Davey, B. H. Li and Z. P. Guo, *Nat Commun*, 2023, **14**, 2720.
37. Y. C. He, W. W. Xue, Y. F. Huang, H. W. Tang, G. X. Wang, D. Z. Zheng, W. Xu, F. X. Wang and X. H. Lu, *Rsc Adv*, 2023, **13**, 15295-15301.
38. Y. C. He, H. W. Tang, Y. F. Huang, K. H. Chen, G. X. Wang, D. Z. Zheng, W. Xu, F. X. Wang and X. H. Lu, *Electrochim Acta*, 2023, **465**, 142988.
39. Z. X. Zhou, M. M. Han, Y. D. Sun, Y. X. Cui, S. A. El-khodary, D. H. L. Ng, J. B. Lian and J. M. Ma, *Adv Funct Mater*, 2024, **34**, 2308834.
40. Z. Y. Yao, W. Zhang, X. C. Ren, Y. R. Yin, Y. X. Zhao, Z. G. Ren, Y. H. Sun, Q. Lei, J. Wang, L. H. Wang, T. Ji, P. Huai, W. Wen, X. L. Li, D. M. Zhu and R. Z. Tai, *ACS Nano*, 2022, **16**, 12095-12106.
41. Y. Q. Du, B. Y. Zhang, W. Zhou, R. K. Kang, W. Y. Zhang, H. X. Jin, J. Q. Wan, J. Y. Qin, J. X. Zhang and G. W. Chen, *Energy Storage Mater*, 2022, **51**, 29-37.
42. B. Wang, J. P. Yan, Y. F. Zhang, M. H. Ye, Y. Yang and C. C. Li, *Adv Funct Mater*, 2021, **31**, 2102827.